Arabian Journal for Science and Engineering (2019) 44:10169–10179
https://doi.org/10.1007/s13369-019-04083-3

RESEARCH ARTICLE - MECHANICAL ENGINEERING

A Novel Three-Dimensional Inverse Method for Axial Compressor Blade Surface Design

Chen Yang[1] · Hu Wu[1] · Yan Liang[1]

Received: 16 November 2018 / Accepted: 30 July 2019 / Published online: 21 August 2019

Abstract
A novel three-dimensional inverse method based on the time-accurate solution of Navier–Stokes equations for axial compressor design is proposed in this work. The main novelty lies in the derivation of an inverse design boundary condition established on the conservation of Riemann invariant in order to directly design the blade surface. Specifically, a dynamic mesh technique is employed to update the grids and reduce the computational costs. In addition, some restrictions are imposed on the blade surface movement in order to avoid unrealistic airfoil profiles and guarantee computational robustness. Two redesign procedures are presented, including shock wave strength restrain for the NASA Rotor 37 stage and integrated controlled diffusion airfoil concept design for the Stage 35. Results indicate that this novel inverse method is effective for detailed axial compressor design.

Keywords Computational fluid dynamics · Inverse method · Axial compressor · Blade design · Dynamic mesh technique

Abbreviations

2D	Two-dimensional
3D	Three-dimensional
CDA	Controlled diffusion airfoil
CFD	Computational fluid dynamics
CFL	Courant–Friedrichs–Lewy
LU-SGS	Lower–upper symmetric Gauss–Seidel
MCA	Multiple circular arc airfoil
NURBS	Non-uniform rational B-spline
RANS	Reynolds-averaged Navier–Stokes equations

1 Introduction

Great progress on the theory of three-dimensional (3D) computational fluid dynamics (CFD) has been achieved during the past thirty years. The flow details captured by CFD simulations can be utilized to redesign the original blade in order to improve the performance of the turbomachinery or eventually achieve the goal of an optimization to the aircraft engine. Therefore, CFD plays an important role in the design area. It is often integrated with some optimization algorithms to redesign or optimize a blade profile. This results in an urgent need for accurate and fast CFD techniques which are currently still inefficient. Due to this, the three-dimensional inverse method may be much more appropriate for design problems.

Some clear and well-understood inverse design methods were first proposed based on the solution of the two-dimensional (2D) potential flow or quasi-3D through flow equations. Sanz [1] developed a numerical automation procedure combined with an inverse hodograph method for the design of controlled diffusion blades. The NASA Lewis inverse design code (LINDES) was then developed [2]. Since sophisticated modern CFD techniques gradually show advantages in predicting viscous turbulent flows, some inverse methods entirely based on 2D or 3D CFD techniques have been developed and proved to be quite effective. Dang [3–5] proposed an inverse method which used a pressure-loading boundary condition across the blade surfaces. Modification of the blade geometry was achieved by specifying a flow-tangency condition along the blade surfaces. Daneshkhah and Ghaly [6] solved the time-accurate RANS equations for design purposes in 3D flows. The developed inverse method was further implemented into a commercial CFD program, namely, ANSYS-CFX, by Arbabi et al. [7]. Qiu et al. [8] established a novel inverse boundary condition, which

✉ Hu Wu
wuhu@nwpu.edu.cn

[1] School of Power and Energy, Northwestern Polytechnical University, Xi'an, China

greatly enhanced the robustness, especially in the presence of tip clearance flow. Roidl and Ghaly [9] prescribed the mass-averaged swirl distribution and the blade thickness distribution to develop an inverse method for turbomachinery cascades. The approach of Van Rooij et al. [10–12] made a reformulation of the inverse method, which effectively decouples the inverse method from the CFD flow solver. Zangeneh et al. [13–15] developed an inverse design system utilizing unstructured grids and the commercial software Turbodesign. Their method was employed by Watanabe and Zangeneh [16] to redesign a forward sweep fan and achieving significant improvements in terms of adiabatic efficiency and choke mass flow. Sun et al. [17] established an applicable airfoil/wing inverse design method with the help of artificial neural networks and airfoil/wing database, which is highly dependent on the accuracy of the trained network and the richness of the database. A ball-spine inverse design algorithm was adapted to an axisymmetric viscous solver by Shumal et al. [18] to optimize the performance of an axisymmetric bend duct, in which the wall pressure distribution was prescribed. Recently, Yang et al. [19] proposed a coupled nonuniform rational B-spline(NURBS) smoothing technique to strengthen the robustness of the inverse method, achieving satisfactory results for several turbomachinery test cases.

It is worth noting that the blade camber is the design variable in most of the CFD-based inverse methods mentioned above. In addition, the blade thickness distribution is prescribed and kept unchanged to allow an easier control for blade shape. However, considering the significant influence of thickness distributions, direct design to blade surface profiles will be a feasible way to further improve the performances. To the writer's knowledge, only Daneshkhah and Ghaly [6] presented an 2D inverse design case using such a scheme. In a similar way, 3D application by Ferlauto was performed in a low speed nozzle guide vane [20] solving incompressible Euler equations. Based on the above analysis, a novel 3D inverse method is developed in this work. The blade suction and pressure side profiles are considered as design variables, while the static pressure distribution on blade surfaces is prescribed as input. A novel inverse design boundary condition based on the conservation of Riemann invariant on the blade surface is proposed. Moreover, spring-based smoothing dynamic mesh technique is adopted to avoid updating the mesh at every iteration in the inverse design, that makes the method quite effective.

The remainder of this paper is organized as follows. Section 2 presents basic governing equations and detailed theory of the proposed inverse method, the derivation process for the novel inverse boundary condition, calculation principle for the inverse design time step, some treatments to improve robustness and the spring-based smoothing dynamic mesh technique. Then, a general inverse design procedure is described in Sect. 3. Its effectiveness is validated in two application cases in Sect. 4, including the shock wave restraining for the NASA Rotor 37 and CDA concept redesign for the stator of NASA Stage 35. Finally, concluding remarks are summarized in Sect. 5.

2 The Novel Inverse Method

2.1 Introduction to Flow Analysis Solver

The inverse method is basically developed on the basis of fully three-dimensional Reynolds-averaged CFD solver. The conservation form of RANS equations in Cartesian coordinates is employed as

$$\frac{\partial}{\partial t}\int_{\Omega} W \,\mathrm{d}\Omega + \int_{\partial\Omega} (F_c - F_v)\,\mathrm{d}S = \int_{\Omega} Q \,\mathrm{d}\Omega \tag{1}$$

where Ω represents the control volume, W are conservative variables, F_c are convective fluxes, F_v correspond to viscous fluxes and Q are source terms. Based on cell-centered finite volume scheme method, both the JST(Jameson, Schmidt, Turkel) central scheme [21] and the Steger–Warming upwind scheme [22] are available to complete spatial discretization, while the explicit hybrid multistage Runge–Kutta scheme or the implicit Lower–Upper Symmetric Gauss–Seidel (LU-SGS) scheme [23] can be used to deal with temporal discretization. As for turbulence model, considering the solving efficiency of inverse design module, a classic Baldwin–Lomax turbulence model [24] is utilized. Two acceleration methods are applied in the solver, namely local-time stepping and central implicit residual smoothing, and the latter is only used with the explicit scheme. Except for some common boundary conditions such as inlet, outlet and periodic ones, mixing plane model [25] is applied to consider the mutual interference between rotor blades and stator blades in a multistage environment. Structured H-type grid is employed to discretize the computational domain. Based on the relevant theories and models above, a program consisting of decoupled direct analysis module and inverse design module has been developed.

2.2 The Novel Inverse Boundary Condition on Blade Surface

In the analysis module, the wall boundary is fixed during the iterations. However, in the inverse module, the fixed-wall boundary condition is replaced by a moving-wall boundary condition. On the basis of the flow solver described above, the core problem of inverse design method is to establish a relationship between prescribed aerodynamic parameters and blade geometry. In the present work, static pressure dis-

tribution on both pressure and suction sides of blade surfaces are prescribed and chosen to calculate the virtual velocity of the blade surfaces. All viscous effects are considered, and a strict non-slip wall boundary condition is implemented.

In the current inverse method, it is assumed that each grid cell line on the blade surface is a one-dimensional subsonic outlet boundary of the flow domain. Then, the outgoing one-dimensional Riemann invariant on the normal direction of the calculation domain can be employed to build a relationship between the prescribed static pressure and the blade wall movement.

$$R^{\pm} = v_n^{\pm} \mp \frac{2a^{\pm}}{\gamma - 1} \tag{2}$$

The superscripts '+' and '−' identify the lower and upper boundaries of the blade surfaces, respectively, and v_n is the virtual velocity normal to the boundary. R is the outgoing Riemann invariant, γ is the specific heat ratio and a is the local sound speed. According to the characteristic theory of one-dimensional isentropic flow, the Riemann invariant remains unchanged when enforcing the inverse boundary condition. For example, on the lower boundary

$$R^{-} = \left(R^{-}\right)^{\text{new}} \tag{3}$$

With the definition of Riemann invariant, Eq. 3 concretely means

$$v_n^{-} + \frac{2\sqrt{\gamma p^{-}/\rho^{-}}}{\gamma - 1} = \left(v_n^{-} + \frac{2\sqrt{\gamma p^{-}/\rho^{-}}}{\gamma - 1}\right)^{\text{new}} \tag{4}$$

It is assumed that ρ is kept constant during the process of inverse design. For a non-slip wall boundary, the normal velocity v_n on the blade surface is zero before blade surface modification. Hence, Eq. 4 becomes

$$\left(v_n^{-}\right)^{\text{new}} = \frac{2}{\gamma - 1}\sqrt{\frac{\gamma}{\rho^{-}}}\left(\sqrt{p^{-}} - \sqrt{\left(p^{-}\right)^{\text{new}}}\right) \tag{5}$$

p^{new} is the prescribed static pressure in the inverse design, which is imposed on the blade surface. ${v_n}^{\text{new}}$ can be interpreted as the blade surface virtual moving velocity, through which the change from the old pressure p to p^{new} could be satisfied. It is clear from Eq. 5 that if a p^{new} equal to p is achieved, then ${v_n}^{\text{new}}$ will be zero and the movement of blade geometry vanishes, which means the goal of the inverse design is achieved. A similar result can be obtained on the upper surface of the blade

$$\left(v_n^{+}\right)^{\text{new}} = \frac{2}{\gamma - 1}\sqrt{\frac{\gamma}{\rho^{+}}}\left(\sqrt{\left(p^{+}\right)^{\text{new}}} - \sqrt{p^{+}}\right) \tag{6}$$

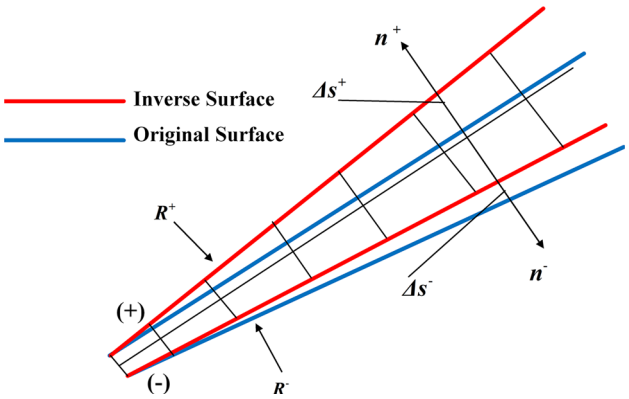

Fig. 1 Inverse boundary condition on blade surfaces

A sketch map of this novel inverse design boundary condition on blade surfaces is given in Fig. 1.

2.3 The Inverse Design Time Step Calculation

The blade wall movement can be calculated by

$$\Delta s = v_n^{\text{new}} \Delta t \tag{7}$$

where Δt is a pseudo time step and it strongly influences the stability of the inverse design procedure. In this method, the suggested value of Δt is nearly on the same order of magnitude as the local time step of time-marching analysis. The detailed method to calculate virtual time step is described as follows

$$\begin{cases} v_{\max} = \max\left(v_i\right) \\ \Delta t_{\text{profile}} = \left(1/\beta_\gamma\right)\min\left(C/n_k, T/n_j\right)/v_{\max} \\ \Delta t = \min\left(\Delta t_{\text{CFL}}, \Delta t_{\text{profile}}\right) \end{cases} \tag{8}$$

β_γ is the stagger angle of the design section, C is the chord of the blade and T is the pitch of the blade row, n_k is the number of grid points in axial direction and n_j is the number of points in tangential direction. Δt_{CFL} is the time step related to Courant–Friedrichs–Lewy (CFL) number in analysis module.

2.4 Robustness Improvements

During the design procedure, several blade sections, i.e., at various spans, are chosen as the design sections and the wall displacement between two design sections is interpolated as shown in Fig. 2. Both the blade pressure and suction side profiles change constantly until the desired static pressure distribution is obtained. For sections nearby the endwall, extrapolation is used because it is hard to provide an accurate

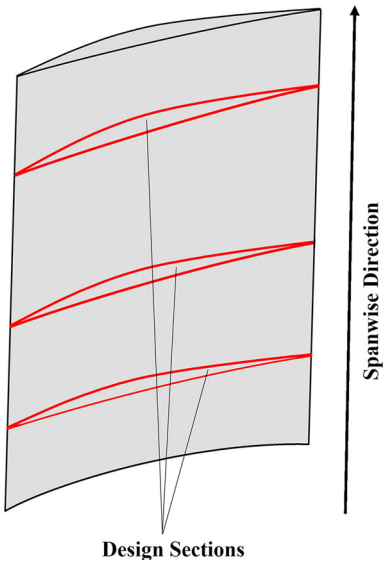

Fig. 2 Blade design sections

static pressure distribution in the absence of endwall boundary layer, which may cause a divergence.

For feasible design, i.e., in order to ensure that there is no intersection or bifurcation on leading or trailing edge, it is necessary to restrict the changing thickness during the inverse design procedure. Firstly, the thickness of leading and trailing edges stays unchanged so as to avoid distortion. In the present work, the leading and tailing edges are not considered as design parameters and are imposed to the updated blade in every inverse design iteration step, i.e., the leading and tailing edges are first translated to the updated blade and then rotated based on the inlet or outlet angle of the updated blade. Secondly, according to some special design intents such as the strength of blades, the upper limit and the lower limit of the blade thickness are input to the inverse design process, as schematically depicted in Fig. 3.

After the calculation of the wall movement for blade surfaces, the new blade surface profiles are defined. In the present work, a radial grid line is selected as the stacking line. The new coordinates of blade profiles are integrated

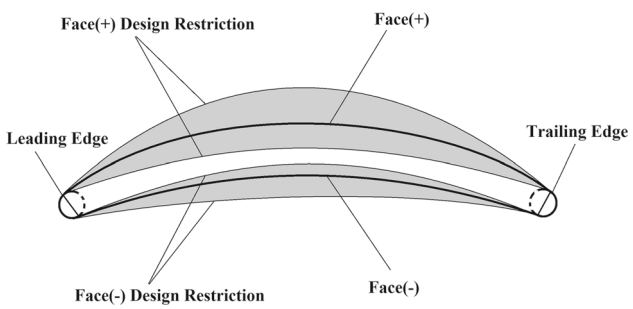

Fig. 3 Blade thickness restriction

upstream and downstream from this line. The upstream coordinates from stacking line are given by

$$\left(s_{i,j}\right)_{\text{new}} = \left(s_{i+1,j}\right)_{\text{new}} + \Delta s_{i,j} + \left(s_{i,j} - s_{i+1,j}\right)_{\text{old}} \tag{9}$$

where $\Delta s_{i,j}$ is the local wall grid movement calculated by Eq. 7. Similarly, downstream coordinates from stacking line are

$$\left(s_{i,j}\right)_{\text{new}} = \left(s_{i-1,j}\right)_{\text{new}} + \Delta s_{i,j} + \left(s_{i,j} - s_{i-1,j}\right)_{\text{old}} \tag{10}$$

2.5 The Spring-Based Smoothing Dynamic Mesh Technique

It is common that in most inverse design methods, the grids of the computational domain need to be regenerated after the blade geometry update at each iteration. However, this is cumbersome and time-consuming considering the high complexity of the 3D mesh topology, which is significantly detrimental to the efficiency of the inverse design. Owing to the unsteady form of the governing equations and the changing blade geometry, it is possible to utilize dynamic mesh modification to overcome this difficulty. Such a technique is widely used in unsteady numerical simulations, while usually they are not necessary for steady calculations in turbomachinery. Nevertheless, it is appropriate to use dynamic mesh in an inverse design problem since the geometry keeps changing until the calculation converges. In this work, spring-based smoothing method is employed to generate a new mesh in the deforming regions, which is interpreted in detail below.

In a spring-based smoothing model, every grid line in the computational domain is regarded as a spring. All of the grid mesh points are in equilibrium state before blade changing. While blade geometry is modified, an external force corresponding to the displacement of the blade will act on all of the springs. Therefore, the length of all springs will be changed until all of the mesh points come to a new equilibrium state which is exaggeratedly exhibited in Fig. 4. According to Hooke's law, forces acting on each grid points in the computational domain can be calculated as

$$(F_N)_i = \sum_{j=1}^{n} k_{i,j}\left(\Delta s_j - \Delta s_i\right) \tag{11}$$

where Δs_i is the displacement of the local grid point i, while Δs_j is the displacement of the adjacent point j. n denotes the total number of grid points adjacent to point i. For structured hexahedron mesh, n equals 6. k is Hooke coefficient, which, according to the literature, can be calculated by

$$k_{i,j} = \frac{1}{\sqrt{\left|l_{i,j}\right|}} \tag{12}$$

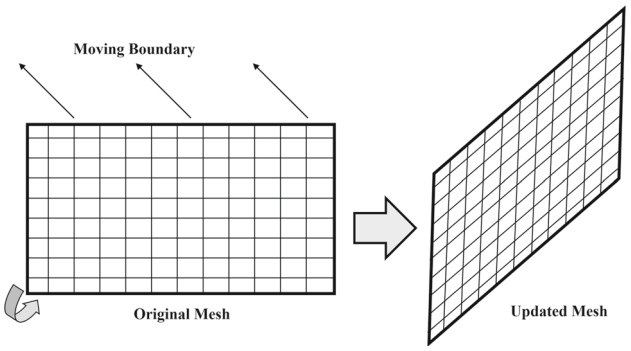

Fig. 4 Spring-based smoothing mesh update

where l denotes the length between adjacent grid lines. Then, the displacement of each grid point can be iterated by means of a point implicit Jacobi method as

$$(\Delta s_i)^{m+1} = \frac{\sum_{j=1}^{n} k_{i,j} (\Delta s_j)^m}{\sum_{j=1}^{n} k_{i,j}} \tag{13}$$

Based on the displacement of the blade surface boundaries at the current time step, the displacement of every grid point can be iterated by Eq. 13 successively until all of the mesh points come to a new equilibrium state. The new coordinates of each grid point can be established by adding the original grid coordinates and the corresponding displacement. Using the spring-based smoothing dynamic mesh technique, the mesh update usually takes less than 10% of CFD run time.

3 Execution Procedure of the Novel Inverse Design Method

Lying in the foundations established above, a general inverse design procedure is developed. At the beginning of the inverse design, the initial blade geometry and the target static pressure distributions on both the lower and upper surfaces are defined. Then, a 3D CFD simulation is carried out. After the analysis module, the inverse design module is executed, in which the virtual displacements of the blade surfaces are computed. Once the displacements at current time step are known, the blade geometry, i.e., its lower and upper surfaces are updated, followed by the spring-based dynamic mesh update. Eventually, the convergence is checked. A typical flow chart for the present inverse design method is shown in Fig. 5. It is noticeable that at the beginning, the selection and definition of the target pressure distributions are based on designer's experiences in fluid mechanics in conjunction with the specific design intent. Considering the high complexity of pressure distributions in a 3D flow, the target pressure distributions are usually based on the pressure distributions

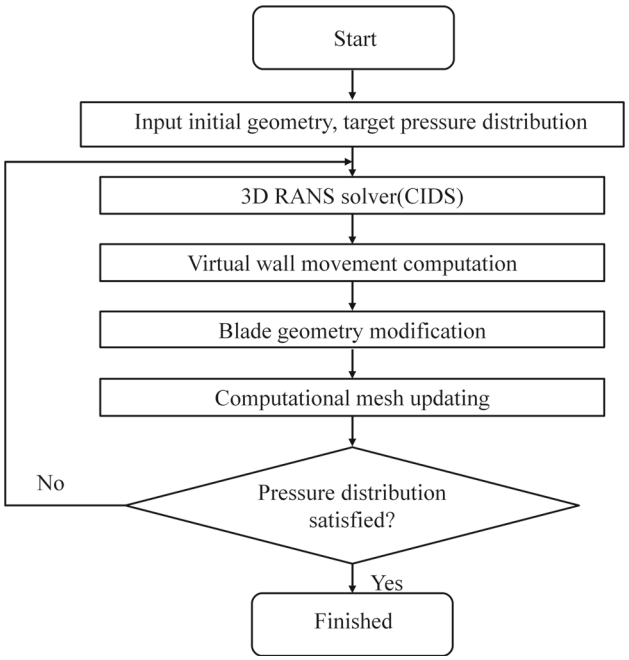

Fig. 5 Flowchart of the present inverse design method

in original blades with some experienced adjustments in practice.

4 Application of the Inverse Design Method

The accuracy of this developed inverse method has been validated by means of a blade recovery test in [26]. Two application cases are presented herein to demonstrate its effectiveness, including the restraining shockwave boundary layer interaction in Rotor 37 stage and the CDA concept redesign of the stator in Stage 35. The spring-based smoothing dynamic mesh technique and treatments to improve the robustness of the method are also applied in these two examples.

4.1 Rotor 37's Shockwave Boundary Layer Interaction Restraining

Rotor 37 is a typical supersonic axial compressor rotor, in which the inlet relative Mach number along the whole span is greater than 1.0. Compared with Rotor 67, Rotor 37 has a higher design pressure ratio of 2.105 [27]. Such considerably high load contributes to its severe flow separation, which has been proved by many experiments and numerical analysis in the past [28,29]. These experiments and simulations showed a typical flow separation caused by interaction between the shock wave and boundary layer which is a complex flow phenomenon. Nevertheless, the strong adverse pressure gradient in the boundary layer caused by the shock wave is definitely the main cause of an imminent risk of separa-

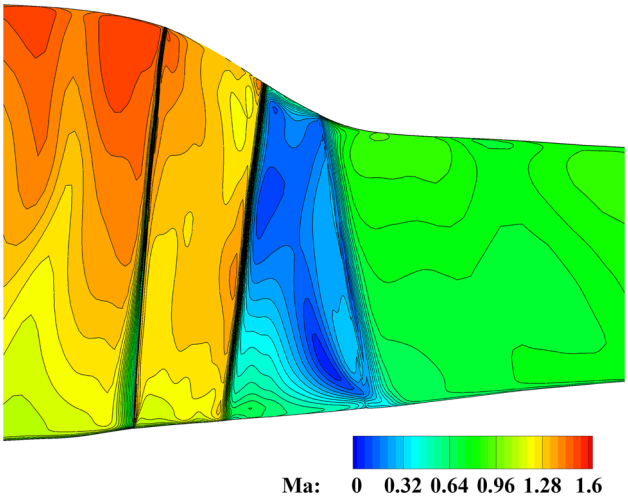

Fig. 6 Rotor 37-relative Mach number contour close to the suction side

tion. Figure 6, in the meridional plane, shows the relative Mach number contours nearby the suction side of Rotor 37 produced by numerical simulation. Behind the shock wave, a sharp decrease in the relative Mach number is observed, especially above 50% span where it almost reduces to zero and is obviously lower than a reasonable value that clearly reveals the flow separation phenomenon.

This redesign work has been conducted with the view of weakening the strength of the shock wave. Based on the flow character and the previous analysis, two design strategies are presented here. According to the first one, the static pressure in front of the shock wave is increased aiming to reduce the shock strength. According to the second one, the pressure rise is maintained almost invariant and the gradient of the static pressure across the shock wave is suppressed. Both make the pressure rise change process gentler so as to decrease the flow loss. The 70% and 90% spanwise locations are chosen as design sections here. The computation iterates about 8000 steps, and the CPU time costs 4 hours approximately on an Intel I7-4790K processor. Figure 7 shows the chordwise static pressure distributions of the original Rotor 37, the target one and the redesign result, at 70% and 90% spanwise locations. The gradient of the static pressure has been suppressed. It is clear that the inverse redesigned result has obtained a conformity with the target pressure distribution satisfactorily.

Figure 8 presents the comparison of blade profiles between original Rotor 37 and redesigned blade. It can be seen that the blade stagger angle changes obviously at 70% span, while it changes less at 90% span. Thinner blade profiles can also be observed at both 70% and 90% span positions.

Figure 9 shows relative Mach number contour comparison at 70% span position, Fig. 9a corresponds to the direct analysis result at the original Rotor 37 blade, while Fig. 9b corresponds to the result of the redesigned blade. In Fig. 9a,

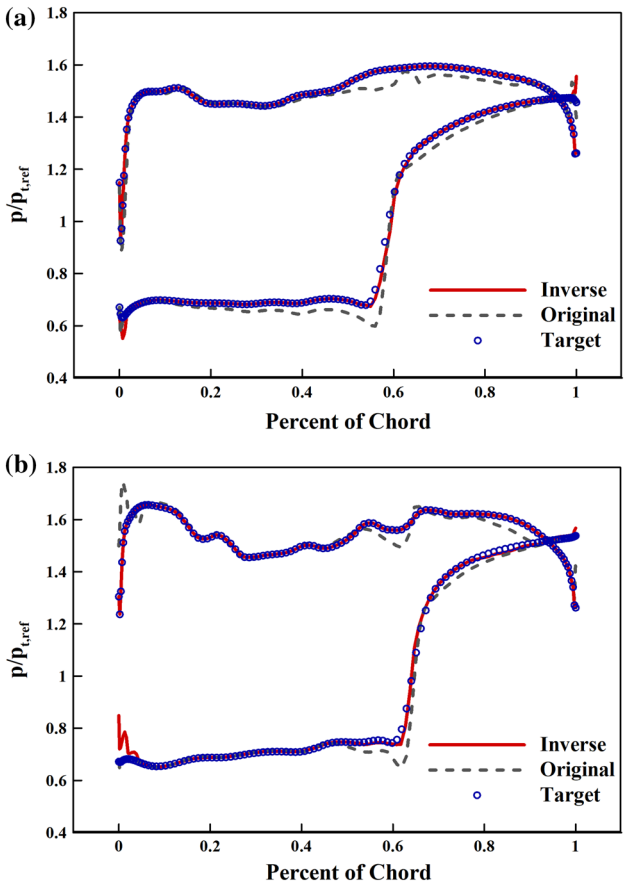

Fig. 7 Rotor 37-static pressure distribution in the inverse design **a** 70% span, **b** 90% span

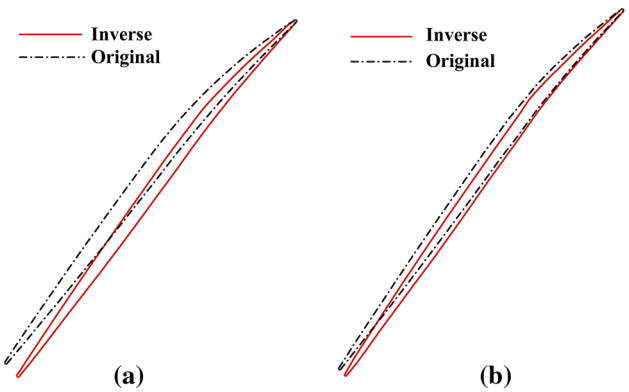

Fig. 8 Rotor 37-profiles of original and designed blade **a** 70% span, **b** 90% span

it can be seen that the boundary layer in suction side begins to grow up from leading edge. However, its growth speed is very slow in front of the shock wave owing to a accelerating flow. Behind the shock wave, the boundary layer thickness is increased sharply due to the strong adverse pressure gradient. Then combined with action of curvature change, it results in flow separation in the original blade. In Fig. 9b, it is obvious

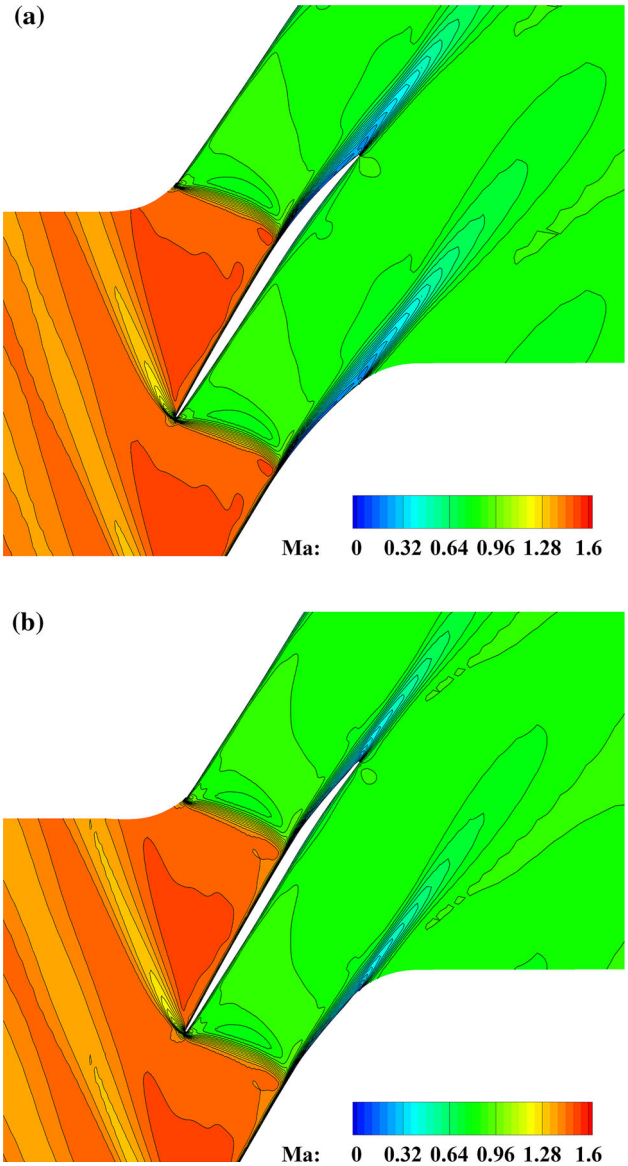

Fig. 9 Rotor 37-relative Mach number contour comparison **a** original blade, **b** redesigned blade

that most of the flow separation has been restrained in the redesigned blade.

Table 1 shows primary aerodynamic performance comparison between original Rotor 37 and redesigned blade. Owing to a more reasonable static pressure distribution, the flow condition has been greatly improved. Compared to the original Rotor 37, the mass flow is increased by 0.77%, the pressure ratio is increased by 2.22% and the adiabatic efficiency is increased by 1.14%.

4.2 Stage 35 Stator Redesign with the CDA Concept

The controlled diffusion airfoil is a kind of airfoil introduced by Hobbs and Weingold [30], which is designed analytically to be shock-free at transonic flows and to avoid suction surface boundary layer separation for a range of inlet conditions. Different from some traditional standard series airfoils, such as NACA65, the thickness distribution of CDA varies with specific flow condition. Usually, there are two kinds of design methods for CDA blade, i.e., the optimization method and the inverse method. The optimization method sets a prescribed velocity distribution as the objective function, which requires a massive calculation to establish a sample database. The inverse design method for a CDA, in contrast, imposes a given surface velocity distribution which reflects the desired aerodynamic behavior. In the early inverse design method, based on the potential equations, systems of nonlinear multi-variable equations were built between the velocity distribution and the blade geometry and then solved by Newton–Raphson iteration method. Compared to the potential method, the 3D RANS method has obviously many advantages, such as much more reliable prediction capability. The newly developed 3D viscous inverse design method is thus utilized in the CDA redesign for Stage 35. Notice that flow velocity on the blade surface is zero in the actual 3D viscous flow. Instead, the isentropic Mach number is adopted to describe the flow near the blade surface. In the present work, the isentropic Mach number distribution is modelled by means of a cubic spline. The corresponding static pressure distribution on blade surface is then computed from the isentropic flow relations, which is used as input of inverse design module.

Table 1 The aerodynamic performance of the original and redesigned Rotor 37

Parameters	Original	Redesigned	%Increase
Mass flow	20.82	20.98	0.77
Pressure ratio	2.120	2.167	2.22
Adiabatic efficiency	0.877	0.887	1.14

Stage 35 is one of the four inlet stages for an advanced core compressor in reference [27], which has a rotor aspect ratio of 1.19 and a staged pressure ratio of 1.82. The stator in Stage 35 is chosen here to achieve a redesign work by applying the CDA concept. The inlet Mach number for the stator varies from 0.725 at the tip to 0.765 at the root. The original stator is designed using multiple circular arc airfoil (MCA) with 46 blades. The tip solidity is 1.3, and the aspect ratio is 1.26. In the present inverse design module, 5, 30, 50, 70 and 95% spanwise locations of the stator are chosen as design sections. It is worth to notice that the inverse design process is running in a stage environment, instead of an isolated stator simulation.

For a stator row in the axial compressor, to achieve a certain exit flow angle is necessary, which means that the exit flow angle should maintain stable through a redesign process.

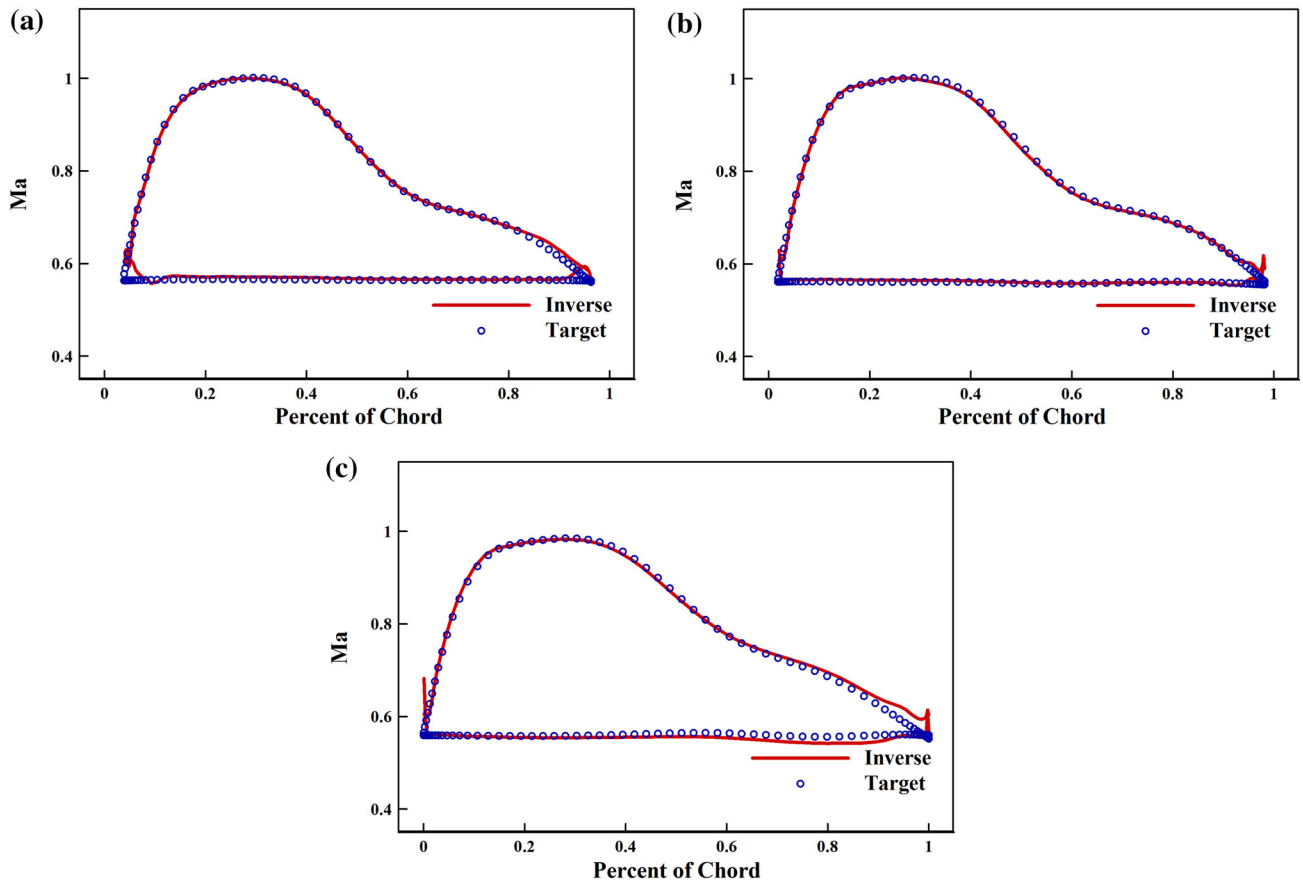

Fig. 10 Stage 35-isentropic Mach number distribution in the inverse design **a** 30% span, **b** 50% span, **c** 70% span

Inspired by the work of Dang et al. [31], this is feasible by a reasonable blade pressure-loading distribution illustrated below. The angular momentum-force balance relationship for a quasi-3D blade element can be expressed as

$$\int_{LE}^{TE} r\,\Delta p\,\mathrm{d}A_\theta = m\left[r_1 V_{\theta,1} - r_2 V_{\theta,2}\right] \tag{14}$$

The pressure loading Δp is the static pressure difference between the pressure side and suction side. Subscripts LE and TE denote the leading and trailing edges of blade, respectively. A_θ is the circumferential projection of the blade camber surface area, m is the mass flow rate through the blade element and $V_{\theta,1}$ and $V_{\theta,2}$ are mass-averaged circumferential velocity at the inlet and outlet, respectively. Once the inlet aerodynamic parameters are fixed, the desired exit flow angle can be obtained by adjusting the pressure loading on the blade surfaces. Specifically, it is necessary to guarantee that the pressure loading of the redesigned blade is equal to the original one on different design sections as the new static pressure distribution is specified.

Figures 10 and 11 show the target Mach number and corresponding static pressure distributions at three of the five different spanwise locations. On the suction side, the maximum Mach number is 1.0, and the strong velocity gradient is avoided so that the risk of an imminent shockwave boundary layer interaction can be eliminated. The Mach number at blade trailing edge on pressure side is 0.56. The design calculation was started using a previous analysis result as the initial solution. The flowfield and blade profile reached its steady state after about 2000 iterations, and the CPU time costs about 3 hours. It is also shown that the target and inverse designed pressure distributions match perfectly in most part of the chordwise. However, the notable deviation can be found nearby the leading and trailing edges. The reason is that in the present inverse design method, leading and trailing edges are not allowed to be redesigned, and thickness at these regions remains unchanged during the inverse design process as described previously. In spite of the inevitably small deviation at the leading and trailing edges regions, the design results can hardly be affected.

Figure 12 presents the comparison at three different locations between new CDA blade profiles designed by the novel inverse method and the original MCA blade. The difference is obvious that the new designed CDA blade has its unique profile and thickness distribution. Over the first half chord,

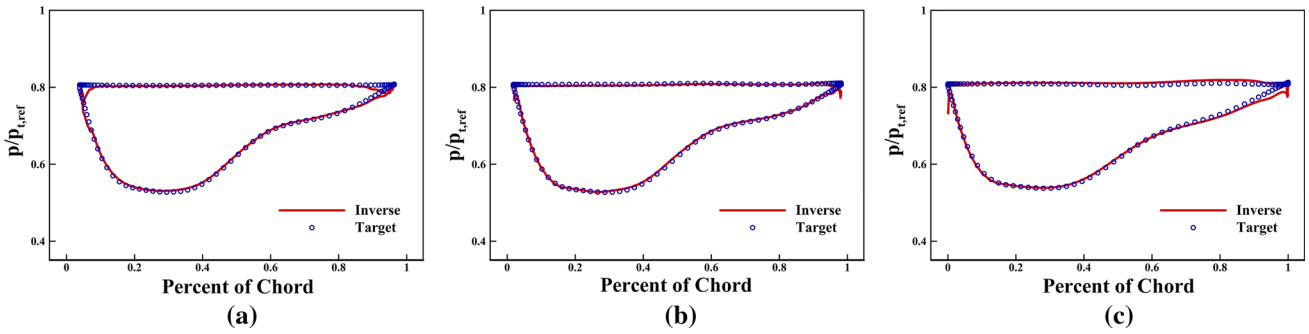

Fig. 11 Stage 35-static pressure distribution in the inverse design **a** 30% span, **b** 50% span, **c** 70% span

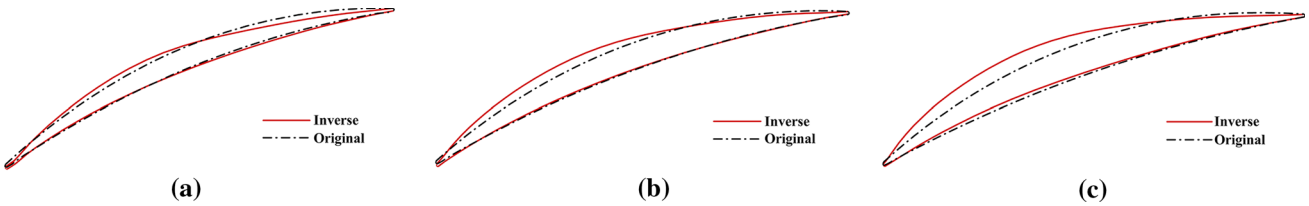

Fig. 12 Stage 35-profiles of original and redesigned blade **a** 30% span, **b** 50% span, **c** 70% span

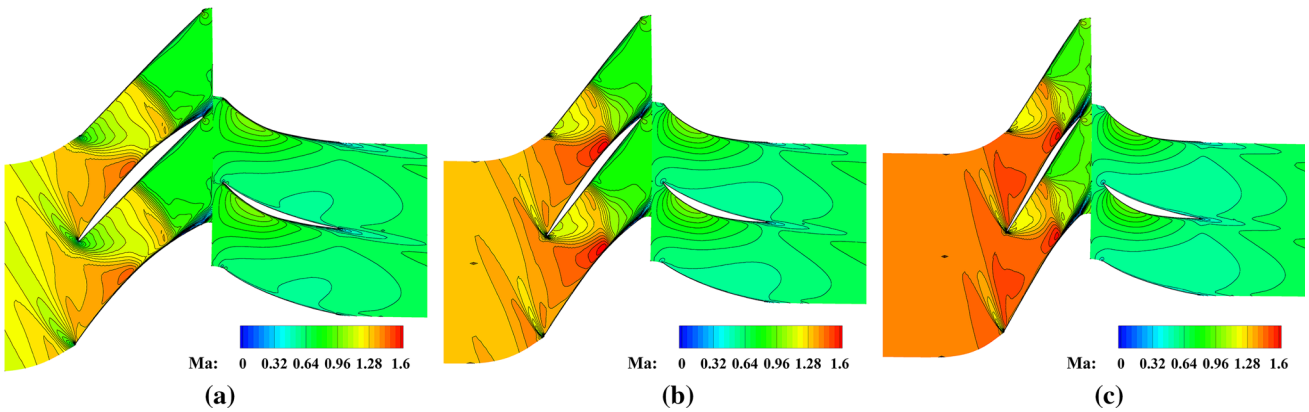

Fig. 13 Stage 35-relative Mach number contour of the designed blade **a** 30% span, **b** 50% span, **c** 70% span

the new designed CDA blade has a greater change in curvature, due to the higher design load. The relatively straight rear half of the blade is necessary to achieve a smooth diffusion process. In contrast, the original blade has a much gentler and even nearly constant curvature change rate.

The relative Mach number contour lines at different spanwise locations are shown in Fig. 13. The stator blade passage flow structure is similar from the root to the tip of the blade. On the suction side, the inlet flow Mach number is about 0.7. The flow accelerates from the leading edge to the peak Mach point with a value very close to 1.0. Then, the flow continues to decrease till the trailing edge. The strong shock wave is avoided, and no boundary layer separation occurs. On the pressure side, the flow nearly keeps a constant subsonic Mach number from the leading edge to the trailing edge. Figure 14 shows the comparison of outlet swirl angle between the original and redesigned stator. It is proven that the sta-

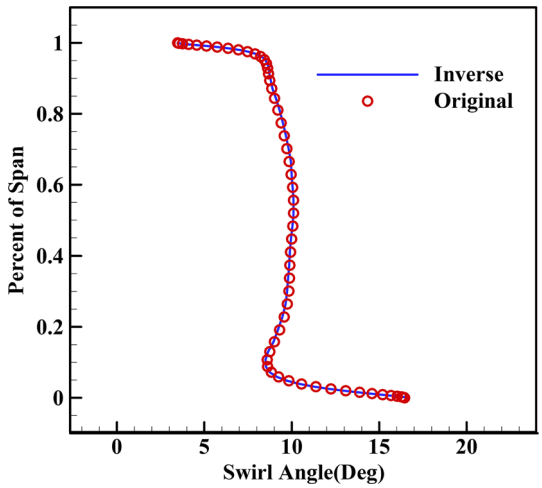

Fig. 14 Stage 35-original and redesigned stator outlet flow swirl angle

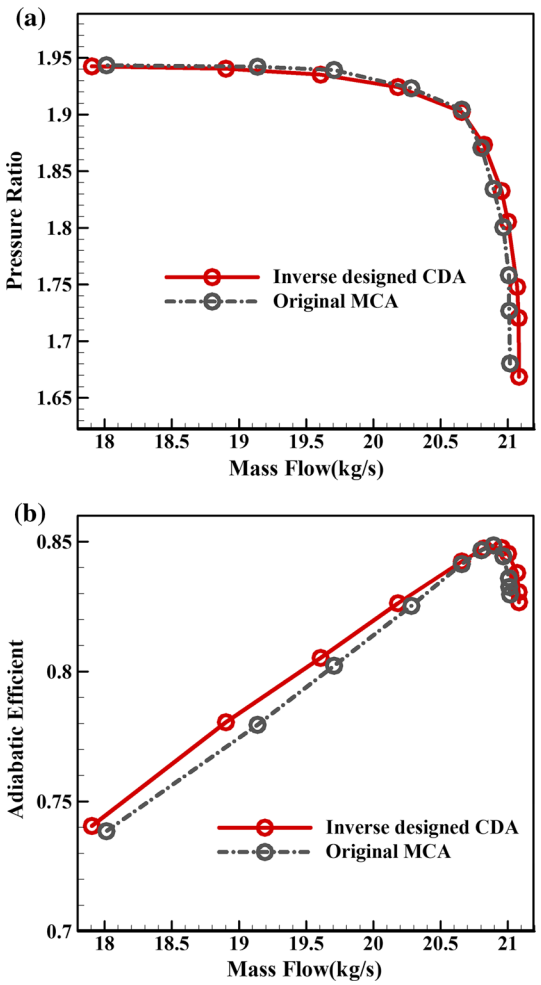

Fig. 15 Stage 35-original and redesigned performance curves **a** absolute total pressure ratio, **b** adiabatic efficiency

tor outlet flow angle stays almost unchanged and the outlet flow environment is 'protected' well by this novel inverse design method. All the results indicate that flow structure of the newly redesigned stator is in good agreement with the CDA concept design qualitatively and quantitatively.

Figure 15 compares the resulting performance curves between the new stage with redesigned CDA stator and the original one. It can be seen that the absolute total pressure ratio performance curves are almost identical. Moreover, it is surprising that almost in the full mass flow range, the adiabatic efficiency of the stage with CDA stator improves significantly compared to the original one, which is not expected at first. This case shows the advantages and potentials of the present inverse method in the region of new concept profiles design. In addition, the direct correlation between the velocity (adiabatic Mach number here) and static pressure makes it possible to use velocity parameters in a 3D inverse design, such as the adiabatic Mach numbers distribution in the Stage 35 case, which is more engineering-friendly and cannot be achieved in a blade camber-designed inverse method.

5 Concluding Remarks

A novel three-dimensional viscous inverse design method has been presented in this work. In this method, a new inverse design boundary condition is developed based on the conservation of the outgoing Riemann invariant normal to the blade surface. It realizes direct update of the blade surface and strict satisfaction of the 'no-slip' boundary condition on it. In addition, a spring-based smoothing dynamic mesh technique is introduced to further improve the inverse design efficiency. Restrictions on blade thickness are also defined to ensure an adequate blade profile and meet some structural strength requirements. Moreover, a detailed inverse design time step calculation method is employed to guarantee a robust design process.

Effectiveness and robustness of this novel 3D inverse design method are demonstrated through two redesign cases concerning the transonic Rotor 37 and the stator in Stage 35. For the Rotor 37 case, the flow separation has been eliminated by restraining the shock wave and boundary interaction; this moderates contradictions between the very high load and the poor aerodynamic performance. Under the nearly same mass flow rate, the inverse redesign increases the total pressure ratio and the adiabatic efficiency by 2.22% and 1.14%, respectively. For the Stage 35 case, the newly defined parameter termed adiabatic Mach number is adopted in the inverse design. Results show nearly the same exit flow angle and absolute total pressure characteristics between the CDA-designed blade and the original one, while the efficiency of the stage is unexpectedly improved in almost the whole mass flow range. This validates the novel inverse design method applied in a stage environment, and enriches the design parameters which can be utilized in 3D inverse design method. In particular, the cases presented in this work indicate that this novel inverse method is robust and effective in compressor redesign. Further applications will be focused on turbine stages, as well as on cases in a multistage environment.

Acknowledgements This work was supported by the National Natural Science Foundation of China (Grant Number 51076131).

References

1. Sanz, J.M.: Automated design of controlled-diffusion blades. J. Turbomach. **110**(4), 540–544 (1988)
2. Sanz, J.M.: Lewis Inverse Design Code (LINDES): Users Manual. NASA Lewis Reasearch Centre, Cleveland (1987)
3. Dang, T.: A fully three-dimensional inverse method fo turbomachinery blading in transonic flows. J. Turbomach. **115**(2), 354–361 (1993)
4. Dang, T.: Inverse method for turbomachine blades using shock-capturing techniques. In: 31st Joint Propulsion Conference and Exhibit, San Diego, CA (1995)

5. Dang, T.; Van, M.P.C.; Larosiliere, L.M.: Design of aspirated compressor blades using three-dimensional inverse method. In: Proceedings of ASME Turbo Expo2003, Atlanta, Georgia (2003)
6. Daneshkhah, K.; Ghaly, W.: An inverse blade design method for subsonic and transonic viscous flow in compressors and turbines. Inverse Probl. Sci. Eng. **14**(3), 211–231 (2006)
7. Arbabi, A.; Ghaly, W.; Medd, A.: Aerodynamic inverse blade design of axial compressors in three-dimensional flow using a commercial CFD Program. In: Proceedings of ASME Turbo Expo 2017, Charlotte, NC (2017)
8. Qiu, X.; Ji, M.; Dang, T.: Three-dimensional viscous inverse method for axial blade design. Inverse Probl. Sci. Eng. **17**(8), 1019–1036 (2009)
9. Roidl, B.; Ghaly, W.: Redesign of a low speed turbine stage using a new viscous inverse design method. J. Turbomach. **133**(1), 2681–2691 (2011)
10. Van Rooij, M.P.C.; Dang, T.; Larosiliere, L.M.: Improving aerodynamic matching of axial compressor blading using a three-dimensional multistage design method. J. Turbomach. **129**(1), 108–118 (2007)
11. Van Rooij, M.P.C.; Dang, T.; Larosiliere, L.M.: Enhanced blade row matching capabilities via 3D multistage inverse design and pressure loading manager. In: Proceedings of ASME Turbo Expo 2008, Berlin, Germany (2008)
12. Van Rooij, M.P.C.; Medd, A.J.: Reformulation of a three-dimensional inverse design method for application in a high-fidelity CFD environment. In: Proceedings of ASME Turbo Expo 2012, Copenhagen, Denmark (2012)
13. Zangeneh, M.; Goto, A.; Harada, H.: On the design criteria for suppression of secondary flows in centrifugal and mixed flow impellers. J. Turbomach. **120**(4), 723–735 (1998)
14. Zangeneh, M.; Goto, A.; Harada, H.: On the Role of three-dimensional inverse design methods in turbomachinery shape optimization. Proc. Inst. Mech. Eng. Part C: J. Mech. Eng. Sci. **213**(1), 27–42 (1999)
15. Tiow, W.T.; Zangeneh, M.: A three-dimensional viscous transonic inverse design method. In: Proceedings of ASME Turbo Expo 2000, Munich, Germany (2000)
16. Watanabe, H.; Zangeneh, M.: Design of the blade geometry of swept transonic fans by 3D inverse design. In: Proceedings of ASME Turbo Expo 2003, Atlanta, Georgia (2003)
17. Sun, G.; Sun, Y.; Wang, S.: Artificial neural network based inverse design: airfoils and wings. Aerosp. Sci. Technol. **42**, 415–428 (2015)
18. Shumal, M.; Nili-Ahmadabadi, M.; Shirani, E.: Development of the ball-spine inverse design algorithm to swirling viscous flow for performance improvement of an axisymmetric bend duct. Aerosp. Sci. Technol. **52**, 181–188 (2016)
19. Yang, J.; Liu, Y.; Wang, X.; et al.: An improved steady inverse method for turbomachinery aerodynamic design. Inverse Probl. Sci. Eng. **25**(5), 633–651 (2017)
20. Ferlauto, M.: A pseudo-compressibility method for solving inverse problems based on the 3D incompressible Euler equations. Inverse Probl. Sci. Eng. **23**(5), 798–817 (2015)
21. Jameson, A.; Schmidt, W.; Turkel, E.: Numerical solutions of the euler equations by finite volume methods using Runge–Kutta time-stepping schemes. In: 14th Fluid and Plasma Dynamics Conference, Alto, CA (1981)
22. Steger, J.L.; Warming, R.F.: Flux vector splitting of the inviscid gasdynamic equations with application to finite-difference methods. J. Comput. Phys. **40**(2), 263–293 (1981)
23. Yoon, S.; Jameson, A.: Lower–upper symmetric-Gauss–Seidel method for the Euler and Navier–Stokes equations. AIAA J. **26**(9), 1025–1026 (1988)
24. Baldwin, B.; Lomax, H.; Thin-layer approximation and algebraic model for separated turbulent flow. In: 16th AIAA Aerospace Sciences Meeting, Huntsville, Alabama (1978)
25. Giles, M.: UNSFLO: A Numerical Method for the Calculation of Unsteady Flow in Turbomachinery. Gas Turbine Laboratory, Massachusetts Institute of Technology, Cambridge (1991). (GTL Report 205)
26. Liu, Z.; Wu, H.: A new three-dimensional viscous inverse design method for axial compressor blade. In: Proceedings of ASME Turbo Expo 2016, Seoul, South Korea (2016)
27. Reid, L.; Moore, R.D.: Design and Overall Performance of Four Highly Loaded, High Speed Inlet Stages for an Advanced High-Pressure-Ratio Core Compressor. Lewis Research Center, NASA, Washington (1978). (NASA-TP-1337)
28. Suder, K.L.: Experimental Investigation of the Flow Field in a Transonic, Axial Flow Compressor with Respect to the Development of Blockage and Loss. Lewis Research Center, NASA, Washington (1996). (NASA-TM-107310)
29. Denton, J.D.: Lessons from rotor 37. J. Therm. Sci. **6**(1), 1–13 (1997)
30. Hobbs, D.E.; Weingold, H.D.: Development of controlled diffusion airfoils for multistage compressor application. J. Eng. Gas Turb. Power **106**(2), 271–278 (1984)
31. Dang, T.; Damle, S.; Qiu, X.: Euler-based inverse method for turbomachine blades, part 2: three-dimensional flows. AIAA J. **38**(11), 2007–2013 (2000)